

# SARS-CoV-2 spike D614G variant exhibits highly efficient replication and transmission in hamsters

**Bobo Mok**

The University of Hong Kong

**Conor J. Cremin**

University of Hong Kong

**Siu-Ying Lau**

The University of Hong Kong

**Shaofeng Deng**

The University of Hong Kong

**Pin Chen**

University of Hong Kong

**Jinxia Zhang**

Department of microbiology

**Andrew Lee**

University of Hong Kong

**HONGLIAN LIU**

The University of Hong Kong

**Siwen Liu**

University of Hong Kong

**Timothy Ting-Leung Ng**

The Hong Kong Polytechnic University

**Hiu-Yin Lao**

The Hong Kong Polytechnic University

**Eddie Lam-Kwong Lee**

The Hong Kong Polytechnic University

**Kenneth Siu-Sing Leung**

University of Hong Kong

**Pui Wang**

University of Hong Kong

**Kelvin To**

The University of Hong Kong <https://orcid.org/0000-0002-1921-5824>

**Jasper Chan**

The University of Hong Kong

**Kwok-Hung Chan**

The University of Hong Kong

**Kwok-Yung Yuen**

University of Hong Kong <https://orcid.org/0000-0002-2083-1552>

**Gilman Kit-Hang Siu**

The Hong Kong Polytechnic University

**Honglin Chen** (✉ [hlchen@hku.hk](mailto:hlchen@hku.hk))

University of Hong Kong <https://orcid.org/0000-0001-5108-8338>

---

## Article

**Keywords:** COVID-19, SARS-CoV-2, viral factors, hamster infection model, transmissibility, pathogenicity

**Posted Date:** September 25th, 2020

**DOI:** <https://doi.org/10.21203/rs.3.rs-81279/v1>

**License:**  This work is licensed under a Creative Commons Attribution 4.0 International License.

[Read Full License](#)

---

1 **SARS-CoV-2 spike D614G variant exhibits highly efficient replication and transmission**  
2 **in hamsters**

3

4

5

6 Bobo Wing-Yee Mok<sup>1</sup>, Conor J. Cremin<sup>1</sup>, Siu-Ying Lau<sup>1</sup>, Shaofeng Deng<sup>1</sup>, Pin Chen<sup>1</sup>, Anna  
7 Jinxia Zhang<sup>1</sup>, Andrew Chak-Yiu Lee<sup>1</sup>, Honglian Liu<sup>1</sup>, Siwen Liu<sup>1</sup>, Timothy Ting-Leung Ng<sup>2</sup>,  
8 Hiu-Yin Lao<sup>2</sup>, Eddie Lam-Kwong Lee<sup>2</sup>, Kenneth Siu-Sing Leung<sup>1</sup>, Pui Wang<sup>1</sup>, Kelvin Kai-  
9 Wang To<sup>1</sup>, Jasper Fuk-Woo Chan<sup>1</sup>, Kwok-Hung Chan<sup>1</sup>, Kwok-Yung Yuen<sup>1</sup>, Gilman Kit-Hang  
10 Siu<sup>2</sup> and Honglin Chen<sup>1\*</sup>

11

12

13 <sup>1</sup>Department of Microbiology and State Key Laboratory for Emerging Infectious Diseases, Li  
14 Ka Shing Faculty of Medicine, The University of Hong Kong, Hong Kong SAR, China.

15 <sup>2</sup>Department of Health Technology and Informatics, Faculty of Health and Social Sciences,  
16 The Hong Kong Polytechnic University, Hong Kong SAR, China

17

18 **\*Correspondence:** hlchen@hku.hk

19

20 **Abstract**

21

22 SARS-CoV-2 causes disease varying in severity from asymptomatic infections to severe  
23 respiratory distress and death in humans. The viral factors which determine transmissibility  
24 and pathogenicity are not yet clearly characterized. We used the hamster infection model to  
25 compare the replication ability and pathogenicity of five SARS-CoV-2 strains isolated from  
26 early cases originating in Wuhan, China, in February, and infected individuals returning from  
27 Europe and elsewhere in March 2020. The HK-13 and HK-95 isolates showed distinct  
28 pathogenicity in hamsters, with higher virus titers and more severe pathological changes in the  
29 lungs observed compared to other isolates. HK-95 contains a D614G substitution in the spike  
30 protein and demonstrated higher viral gene expression and transmission efficiency in hamsters.  
31 Intra-host diversity analysis revealed that further quasi species were generated during hamster  
32 infections, indicating that strain-specific adaptive mutants with advantages in replication and  
33 transmission will continue to arise and dominate subsequent waves of SARS-CoV-2  
34 dissemination.

35

36 **Keywords:** Coronavirus, SARS-CoV-2, COVID-19, Spike, D614G, transmission, hamster

37

## 38 **Introduction**

39 A newly emerged  $\beta$ -coronavirus, SARS-CoV-2, which causes COVID-19 disease in humans,  
40 attained cross species transmission through a process yet to be defined in detail (Andersen et  
41 al., 2020; Wu et al., 2020; Zhou et al., 2020a). Human cases were first identified in Wuhan,  
42 China, in December 2019 and SARS-CoV-2 subsequently disseminated worldwide leading to  
43 the announcement of a global pandemic by the World Health Organization on March 11, 2020  
44 (Mahase, 2020). More than 20 million laboratory-confirmed cases and over 700,000 deaths  
45 have been recorded globally to date (<https://coronavirus.jhu.edu/map.html>) (Dong et al., 2020).  
46 In contrast to SARS-CoV and MERS-CoV, a significant number of SARS-CoV-2 infections  
47 are asymptomatic. However, in areas high virus activity a substantial portion of infections lead  
48 to severe disease or death (Chen et al., 2020b). While aging and certain underlying medical  
49 conditions may predispose individuals to increased severity of COVID-19 disease (Zhang et  
50 al., 2020c), it is not clear if viral factors may also contribute to the variable pathogenicity of  
51 SARS-CoV-2 in humans (Becerra-Flores and Cardozo, 2020). It is expected that SARS-CoV-  
52 2 will continue to be transmitted among humans globally, leading to the emergence of more  
53 phenotypic variants. It is therefore important to define the viral factors associated with  
54 transmissibility and pathogenicity of SARS-CoV-2. Analysis of a mutant virus with a deletion  
55 at the spike protein S1/S2 junction showed that the PRRA polybasic cleavage site is associated  
56 with heightened pathogenicity in the model (Lau et al., 2020b). SARS-CoV-2 is of zoonotic  
57 origin and is currently in the process of becoming more adapted to humans as it circulates and  
58 acquires adaptative mutations. Different variants have already been identified among clinical  
59 specimens and in cultured isolates (Gong et al., 2020; Su et al., 2020). Some deletion or  
60 mutation variants may not be recognized by general sequencing protocols, for which the  
61 readout only shows the dominant population in clinical specimens or cell culture samples, but  
62 can be detected by more sensitive methods (Wong et al., 2020).

63 SARS-CoV-2 was first identified in China in December 2019 (Wu et al., 2020; Zhou et  
64 al., 2020a). A response adopting aggressive control measures, including the lock down of a city  
65 of 10 million people (Wuhan) and the wider Hubei Province (population: 56 million) in January  
66 2020, significantly limited the further dissemination of the virus within China (Ji et al., 2020;  
67 Lau et al., 2020a). SARS-CoV-2 has been efficiently transmitting among humans since it was  
68 first recognized, according to studies from the early outbreak (Chan et al., 2020a; Liu et al.,  
69 2020). Subsequent transmission of SARS-CoV-2 in Europe, the US and other countries has  
70 resulted in more widespread human infections since March 2020. As more humans are exposed  
71 to the SARS-CoV-2 virus, it is expected that more host adapted phenotypic variants of the virus

72 will emerge. It is important to determine whether some emerging variants may have the  
73 potential to go on to become the dominant strain in the coming waves of circulation. Indeed, a  
74 strain bearing a D614G mutation in the spike protein, first observed in January 2020 among  
75 isolates from China and Europe, has since become the dominant population in the recent  
76 transmissions occurring in Europe and the US (Korber et al., 2020). Studies using pseudo-  
77 viruses containing spike genes derived from natural isolates have shown that variants harboring  
78 D614G infect cells more effectively (Daniloski et al., 2020; Zhang et al., 2020b). Although  
79 D614G is in the spike protein, the D614G variant is still susceptible to neutralization by  
80 antibodies raised against strains lacking this mutation (Korber et al., 2020). To further  
81 understand the properties of the D614G variant, we analyzed pathogenicity, virus replication  
82 efficiency and the global transcriptome of the host response in the airways of SARS-CoV-2  
83 D614G variant infected hamsters. Although it is not clear if the D614G variant causes more  
84 severe disease in humans, our data showed that SARS-CoV-2 containing D614G replicates  
85 more efficiently and causes more severe pathological changes in the lung tissues of infected  
86 animals when compared to isolates lacking this mutation.

87

## 88 **Results**

### 89 **SARS-CoV-2 genomic variants exhibit variable pathogenicity in hamsters**

90 Five isolates were selected to study variability in the pathogenicity of SARS-CoV-2  
91 strains and the host response to such variants in a hamster infection model. These strains  
92 represent isolates from the early outbreak in China (HK-8, HK-13 and HK-15) and subsequent  
93 outbreaks in Europe and elsewhere (HK-92 and HK-95) (Table S1). Phylogenetic analysis  
94 revealed that these strains belonged to distinctive GISAID phylogenetic clades (**Figure S1**).  
95 The sequences of these five isolates were compared with that of the index isolate (Wuhan-Hu-  
96 1), characterized during the early outbreak in Wuhan city, China (Wu et al., 2020; Zhou et al.,  
97 2020a), revealing a range of variations in the untranslated region and *Orf1a*, *Orf1b*, *Orf3*, *Orf8*,  
98 *N* and *S* genes among strains (**Table 1**). HK-95 is an isolate characterized from a traveler  
99 returning to Hong Kong from Egypt and carries a D614G substitution in the spike gene (**Figure**  
100 **S1**). Hamsters are a highly susceptible model for studying SARS-CoV-2 infection, with disease  
101 in hamsters closely simulating COVID-19 disease in humans (Chan et al., 2020b). Infection  
102 progresses rapidly in hamsters, but infected animals then recover after about one-week of  
103 infection. We infected hamsters with these five strains of SARS-CoV-2 and monitored disease  
104 presentation for 5 days. All five isolates caused significant body weight loss compared to the  
105 control group (**Figure 1A**). In SARS-CoV-2-infected hamsters, three major histopathological  
106 changes were observed in lungs: various degrees of bronchial or bronchiolar inflammation  
107 (bronchiolitis), lung parenchymal inflammatory damage (alveolitis) and pulmonary blood  
108 vessel inflammation (vasculitis). These pathological changes were most severe at day 5 after  
109 virus inoculation. The HK-13 and HK-95 isolates caused more extensive bronchiolar cell death,  
110 diffuse alveolar space exudation and infiltration and lung consolidation, compared to HK-8  
111 (**Figure 1B**). In our previous report, at day 4 post-infection (pi) with HK-001a virus, alveoli  
112 had already started to show focal areas of cell proliferation indicating resolution of  
113 inflammation (Chan et al., 2020b; Lau et al., 2020b). However, such indications of resolution  
114 were not seen in HK-95- or HK-13-infected hamsters, even at day 5 post-infection, indicating  
115 that the acute lung inflammation caused by both of these strains may last longer than that  
116 triggered by infection with other SARS-CoV-2 strains.

### 117 **Differences in replication rates of SARS-CoV-2 isolates in infected hamsters**

118 Examination of virus titers in lung tissues and nasal washes at day 5 post-infection  
119 showed that HK-13 and HK-95 replicate to significantly higher levels than the other three  
120 isolates (**Figure 2A and S2**). We then analyzed viral gene expression in the lung tissues of  
121 hamsters infected with different isolates using RNA-seq analysis. Consistent with the virus

122 titers, viral gene expression also showed a similar distribution between isolates when  
123 comparing the average expression of all viral genes per isolate (black line) to viral titer profiles  
124 (**Figure 2B**). Interestingly, the expression distribution between each of the viral genes for each  
125 isolate is very similar across all isolates, with differences in overall expression being due to a  
126 proportional change in expression across all genes. This indicates that the observed differences  
127 in viral gene expression can be attributed to isolates maintaining different rates of replication.  
128 These differences in replication suggest that some viral isolates may be more constrained by  
129 host-specific factors and as such are unable to achieve an optimal rate of replication, as is seen  
130 for HK-8. This also implies that individual isolates interact differently with their hosts during  
131 the infection process. To assess if constraints to viral replication are reflected in the severity of  
132 the host response induced by SARS-CoV-2 infection, we performed an initial characterization  
133 of the hamster host response to infection.

#### 134 **Differential expression of SARS-CoV-2 genes and host response in hamsters**

135 To further understand the global host response elicited by difference isolates, we  
136 grouped the samples in a principal component analysis (PCA) (Figure 2C). In this PCA space,  
137 we observed transcriptional perturbations along the two principal components, both account  
138 for more than 25% of sample variation (Figure 2C). This analysis suggested unique expression  
139 signatures in hamster host responses to infection with different SARS-CoV-2 isolates. In  
140 addition, volcano plots show that viral isolates HK-13 and HK-95, which demonstrate higher  
141 rates of replication than isolate HK-8, incited significant upregulation of host gene expression  
142 compared to HK-8 (**Figure 3**). Unsurprisingly, the host responses provoked by HK-8 and HK-  
143 15 were similar, as these isolates share a similar replication rate. These profiles suggest that  
144 higher rates of SARS-CoV-2 replication are a significant driving factor in triggering host  
145 responses, which may associate with greater disease severity in humans (Blanco-Melo et al.,  
146 2020; Zhou et al., 2020b). However, the differential expression profile generated by comparing  
147 HK-8 to HK-92 is similar to that of HK-8 vs HK-95. Since HK-92 has a considerably lower  
148 replication efficiency than HK-95 in hamsters (**Figure 2**), this suggests that factors independent  
149 of the replication of HK-92 are also involved in inducing the significant upregulation of host  
150 gene expression seen here. This offers an explanation as to the close coordinate positioning of  
151 HK-92 to HK-95 in our PCA analysis (**Figure 2C**), and why HK-13 is positioned further away,  
152 despite possessing a similar replication rate to HK-95 (**Figure 2A and S2**). Our analysis has  
153 made it clear that the upregulation of the host response is heavily dependent on the specific  
154 viral SARS-CoV-2 isolate that is causing infection. Although viral replication is a significant

155 driver in stimulating the host response in hamsters, SARS-CoV-2 appears to have developed  
156 replication-independent strategies to influence responses in infected hosts.

157 Hamsters have proven to be a useful live model for studying the dynamics of viral  
158 infection and are now routinely used to assess SARS-CoV-2 pathogenesis (Chan et al., 2020b;  
159 Lau et al., 2020b; Zhang et al., 2020a). However, the current annotation that is available to  
160 describe gene functionality and perform network analysis in hamsters is limited. Therefore, we  
161 opted to use the gene functional annotation of a well-defined animal model within close  
162 evolutionary distance of the hamster. Our evolutionary analysis identified mice as being  
163 suitably closely related to hamsters (**Figure S3**). Therefore, our gene enrichment analysis of  
164 differentially expressed hamster-mouse gene orthologues using mouse Gene Ontology (GO)  
165 annotation is anticipated to give a fair representation of the induced host response to SARS-  
166 CoV-2, without enrichment of redundant hamster-specific processes. GO enrichment analysis  
167 identified many functional groups corresponding to T-cell activation and chromatin remodeling  
168 as being the networks most significantly upregulated by SARS-CoV-2 infection, regardless of  
169 viral isolate used, when compared to samples from uninfected hamsters (**Figure 4**). Activation  
170 of T-cells is indicative of upregulation of the adaptive immune response and the host's attempts  
171 to restrict viral pathogenesis. The upregulation of chromatin remodeling pathways indicates  
172 significant disruption to DNA architecture and an increase in nuclear repair processes,  
173 potentially due to cellular stress caused by the SARS-CoV-2 virus during infection. We also  
174 conducted GO enrichment analysis of differentially expressed genes in hamster lungs induced  
175 by the various SARS-CoV-2 isolates, this time conducting comparisons to samples from HK-  
176 95 hamster infections. Our result indicates that subverted gene networks are subject to strain  
177 specific targeting processes by the more pathogenic strains of SARS-CoV-2, but not by HK-8  
178 (**Figure S4**). Overall, the main effects of SARS-CoV-2 infection involved activation of the T  
179 cell response and disruption of regulatory processes in the nuclear microenvironment of  
180 infected cells.

### 181 **D614G variant demonstrates higher transmissibility in hamsters**

182 Surveillance of the evolution of SARS-CoV-2 during circulation in humans has  
183 identified various mutations which may relate to the infectivity of virus (Chen et al., 2020a;  
184 Korber et al., 2020) The spike D614G variant of SARS-CoV-2 has been the clearly dominant  
185 population since March 2020, suggesting that it has enhanced infectivity in humans (Becerra-  
186 Flores and Cardozo, 2020; Daniloski et al., 2020; Zhang et al., 2020b). We conducted an  
187 experiment using the hamster model to examine if the transmission ability of the HK-95 strain,  
188 which carries spike D614G, may be enhanced compared to two other isolates (HK-8 and HK-

189 13) which lack the D614G substitution (**Figure S5**). Notably, higher virus titers were found in  
190 the lung and nasal turbinate tissues of recipient hamsters co-housed with HK-95-infected  
191 hamsters than in those secondarily exposed to HK-8 or HK-13 (**Figure 5A**), which differs from  
192 the direct infection experiment, where HK-13 and HK-95 demonstrated similar viral titers in  
193 respiratory tissues (**Figure 2A and S2**). We did not examine if naive hamsters in the HK-95  
194 group were infected at an earlier time point than those in other groups due to limited availability  
195 of experimental animals. But given the higher viral titers in the lung and nasal turbinate tissues,  
196 it is possible that hamsters co-housed with a HK-95-infected hamster were infected earlier than  
197 those co-housed with hamsters infected with HK-8 or HK-13, and that this facilitated greater  
198 virus replication in recipients. It is unclear how the D614G mutation affects virus replication.  
199 The efficiency of spike protein cleavage is known to associate with coronavirus replication  
200 (Hoffmann et al., 2020; Jaimes et al., 2020). We found that introduction of the D614G mutation  
201 into the Wuhan-Hu-1 prototype sequence enhanced SARS-CoV-2 spike cleavage in cells  
202 (**Figure 5B**). Since D614G is not located at either of the cleavage sites in the spike protein of  
203 SARS-CoV-2, the molecular basis of this effect remains to be investigated. Taken together,  
204 these results confirm that acquisition of D614G promotes SARS-CoV-2 infectivity in a  
205 mammalian model of SARS-CoV-2 infection.

#### 206 **Intra-host diversity in infected hamsters**

207 To examine intra-host diversity of the different SARS-CoV-2 strains, nasal washes  
208 were collected from infected hamsters at days 3 and 5 post-infection and whole genome  
209 sequencing conducted to determine the stability of the viral genome over the course of infection.  
210 As inferred by Illumina sequencing data, even minor genome variant populations (i.e. variants  
211 with frequency < 0.3) identified in the original inoculating strains (**Table 1**) remained present  
212 after 5 days of infection (**Table S2**). Interestingly, some genome variants, which were absent  
213 in the original strains, developed during hamster infection. The frequencies of these newly  
214 arisen variants were generally higher at 5 dpi than at 3 dpi (**Table S2**). This trend of increase  
215 implied that these new variants survive better in hamsters. Of note, there was no mixed  
216 population observed in HK-95, either in the original isolate or in animals after infection, which  
217 may indicate that the D614G variant has acquired a relatively stable genome constellation for  
218 replication in mammals; this stability in both human isolates and hamster infections also further  
219 supports the contention that hamsters are a suitable model for human SARS-CoV-2 infection.

220

## 221 Discussion

222 SARS-CoV-2 continues to transmit globally and since its emergence in December 2019  
223 has caused more than 20 million laboratory confirmed infections and over 0.7 million deaths,  
224 as of August 26 2020. Social distancing strategies have been adopted to slow down the  
225 dissemination of virus, in hope that effective vaccines and therapeutics will be developed and  
226 available soon enough to prevent further waves of transmission. More than seven months after  
227 transmission in humans was first observed, various genetic variants of SARS-CoV-2 have  
228 emerged and been analyzed but no clear evolutionary direction for SARS-CoV-2 is yet  
229 apparent (Deng et al., 2020; Fauver et al., 2020; Forster et al., 2020; Sanchez-Pacheco et al.,  
230 2020). Since the majority of people remain naive to this virus it is necessary to closely track  
231 any potential changes in the pathogenic properties of SARS-CoV-2 variants along the course  
232 of transmission. SARS-CoV-2 is of zoonotic origin and is expected to gain more adaptations  
233 as it circulates in humans. Attenuated variants with deletions in the spike protein S1/S2 junction  
234 and other regions have been detected in virus-infected cell cultures and in patient specimens  
235 (Lau et al., 2020b; Wong et al., 2020). One variant containing D614G in the spike protein has  
236 become the dominant population in many countries since March 2020 and is reported to infect  
237 cells more efficiently *in vitro* (Daniloski et al., 2020; Li et al., 2020; Zhang et al., 2020b). To  
238 understand if D614G variant virus may exhibit altered pathogenicity and transmissibility, we  
239 compared 5 SARS-CoV-2 isolates obtained from Hong Kong returnees from Wuhan, China,  
240 in February and travelers who had visited Europe and other countries after March 2020, using  
241 the hamster infection model. We found that the D614G bearing strain, HK-95, replicates more  
242 efficiently in the airways of infected hamsters in the lungs than strains lacking D614G (**Figure**  
243 **2 and S2**). A contact transmission experiment showed that naive hamsters exposed to a HK-  
244 95-infected hamster have higher titers of virus in their airways, suggesting that the D614G  
245 variant is more highly transmissible than non-D614G SARS-CoV-2 strains (**Figure 5**).

246 Infection with SARS-CoV-2 can range from being asymptomatic to causing severe  
247 disease and fatalities; it is not yet well understood which viral factors, together with host factors  
248 and conditions, may determine pathogenicity in humans. Besides the insertion of a polybasic  
249 cleavage PRRA motif at the S1/S2 junction of the spike protein, which clearly contributes to  
250 increased virulence features, and was probably responsible for the initial SARS-CoV-2 cross  
251 species transmission event (Andersen et al., 2020; Lau et al., 2020b), other virulence elements  
252 are not well defined. The spike D614G variant, which was first recorded in January in China  
253 (hCoV-19/Zhejiang/HZ103/2020; 24 January 2020) and shortly thereafter in Germany (hCoV-  
254 19/Germany/BavPat1-Chvir929/2020; 28 January 2020), was found to have subsequently

255 become the dominant population in multiple countries, suggesting SARS-CoV-2 is adapting  
256 to become more transmissible in humans. Host adaptation of an emerging virus in a naive  
257 population is generally believed to involve the virus gaining more efficient replicative ability  
258 while gradually decreasing its pathogenicity in the new host. It is not clear if the spike D614G  
259 variant will drive SARS-CoV-2 towards this evolutionary pathway. The more pathogenic  
260 features of the HK-95 strain, which carries the D614G substitution, observed in hamsters in  
261 this study could be due to the high replication efficiency of this strain in animals, given that  
262 hamsters are highly susceptible to SARS-CoV-2 infection. This is consistent with our  
263 transcriptome analysis of lung tissues from infected hamsters, which revealed no significant  
264 difference between host responses to infection with 614D or 614G strains (**Figure 4 and S4**).  
265 However, the contact transmission experiment demonstrated that HK-95 exhibits higher  
266 transmissibility to naive hamsters than HK-13 (**Figure 5**), despite these strains provoking  
267 similar pathogenic effects and transcriptome profiles in infected hamsters (**Figure 1, 2, 4 and**  
268 **S4**). If the spike D614G mutation is joined by other adaptive mutations as the virus further  
269 circulates in humans, it may be postulated that a variant with the D614G substitution together  
270 with a deletion in the polybasic cleavage site at the S1/S2 junction could arise, and if so, it may  
271 present as a much less pathogenic version of SARS-CoV-2 in the aftermath of the COVID-19  
272 pandemic. Nevertheless, human interventions, such as mass vaccination as soon as vaccines  
273 are available, and preexisting immunity from prior infections are likely to drive the evolution  
274 of variants that can evade host immunity.

275         The increased transmissibility of the D614G SARS-CoV-2 strain is likely due to its  
276 higher replication ability. How the spike D614G mutation enhances virus replication and  
277 consequently transmissibility has not been defined. We and others have shown that D614G  
278 variant spike proteins are more efficiently cleaved into S1 and S2 subunits in cells (**Figure 5B**)  
279 (Daniloski et al., 2020; Zhang et al., 2020b). Two synonymous mutations, 5'UTR-C241T and  
280 *Orf1a*-C3037T, and one nonsynonymous mutation, *Orf1b*-P314L, are consistently linked in  
281 D614G variant strains (**Table 1**). It remains to be investigated whether these mutations jointly  
282 contribute to the enhanced replication ability of the HK-95 SARS-CoV-2 isolate. Of note,  
283 *Orf1b*-P314L lies within the RNA-dependent RNA polymerase (RdRp) region, suggesting this  
284 mutation may play a causative role on enhanced viral replication. Further studies, including  
285 structural and functional analyses, will provide necessary information for understanding the  
286 molecular basis underlying the D614G-associated SARS-CoV-2 phenotype.

287  
288

289 **Materials and Methods**

290

291 **Virus**

292 The SARS-CoV-2 isolates HK-8 (MT835139), HK-13 (MT835140), HK-15 (MT835141),  
293 HK-92 (MT835142) and HK-95 (MT835143) were isolated from specimens obtained from five  
294 laboratory-confirmed COVID-19 patients using Vero E6 cells (ATCC; CRL-15786). All  
295 experiments involving SARS-CoV-2 viruses were conducted in a Biosafety Level-3 laboratory.  
296 For animal challenge, viral stocks were prepared after two serial passages of isolated virus in  
297 Vero E6 cells in Dulbecco's Modified Eagle Medium (DMEM) (Thermo Fisher Scientific)  
298 supplemented with 5% fetal bovine serum (Thermo Fisher Scientific), and 100 IU penicillin  
299 G/ml and 100 ml streptomycin sulfate/ml (Thermo Fisher Scientific). Virus titers were then  
300 determined by plaque assay using Vero E6 cells. Viral RNAs were also obtained from the  
301 supernatants of infected cells and then isolated using the QIAamp RNA Viral kit (Qiagen) and  
302 subjected to whole viral genome sequencing.

303

304 **Hamster infection**

305 Female golden Syrian hamsters, aged 8-9 weeks old, were obtained from the Laboratory  
306 Animal Unit, the University of Hong Kong (HKU). All experiments were performed in a  
307 Biosafety Level-3 animal facility at the LKS Faculty of Medicine, HKU. All animal studies  
308 were approved by the Committee on the Use of Live Animals in Teaching and Research, HKU.  
309 Virus stocks were diluted with phosphate-buffered saline (PBS) to  $2 \times 10^4$  PFU/ml. Hamsters  
310 were anesthetized with ketamine (150mg/kg) and xylazine (10 mg/mg) and then intranasally  
311 inoculated with 50 ul of diluted virus stock containing  $10^3$  PFU of virus or 50 ul PBS (mock  
312 infection control). Body weights were monitored daily for 5 days. Nasal washes were collected  
313 from hamsters at 3 and 5 dpi. Total nucleic acid was extracted from 140 ul of sample fluid  
314 using the QIAamp RNA Viral kit (Qiagen) and eluted with 30 ul of DEPC-treated water. Seven  
315 ul RNA was used for reverse transcription using MultiScribe Reverse Transcriptase  
316 (Thermofisher). cDNA was subsequently used for real-time qPCR using TB Green Premix Ex  
317 Taq (Tli RNase H Plus) (Takara). Viral RNA from nasal washes was also used for whole viral  
318 genome sequencing. Hamsters were euthanized at 5 dpi and lung tissues collected for  
319 histopathology, determination of viral load and RNA sequencing.

320

321 **Viral load determination and histopathology**

322 Lung right lobes (superior, middle and inferior) were homogenized in 1 ml of PBS. After  
323 centrifugation at 12,000 rpm for 10 min, the supernatant was harvested, and viral titers  
324 determined by plaque assay using Vero E6 cells. Lung left superior lobes were fixed in 4 %  
325 paraformaldehyde and then processed for paraffin embedding. The 4 µm tissue sections were  
326 stained with haematoxylin and eosin for histopathological examination. Images were obtained  
327 with an Olympus BX53 semi-motorized fluorescence microscope using cellSens imaging  
328 software.

329

### 330 **RNA sequencing of hamster lung tissues**

331 Lung left inferior lobes from hamsters were cut into pieces and lysed using the RA1 lysis buffer  
332 provided with the NucleoSpin® RNA Plus kit (Macherey-Nagel). RNA extraction was then  
333 performed according to the manufacturer's instructions, including an on-column genomic  
334 DNA digestion step. 1 µg of high-quality total RNA (RIN>8) was used for cDNA library  
335 preparation with a KAPA mRNA HyperPrep Kit. The libraries were then denatured and diluted  
336 to optimal concentration, before being sequenced on an Illumina NovaSeq 6000 in a 151bp  
337 Paired-End format. RNA-seq data used in this study can be accessed in GEO under the  
338 accession number GSE156005.

339

### 340 **Transmission experiment**

341 For each virus strain two hamsters were intranasally inoculated with 10<sup>3</sup> PFU of virus. At  
342 twenty-four hours post-infection (1 dpi), each infected donor hamster was transferred to a new  
343 cage and co-housed with three naïve hamsters for 1 day. At 4 dpi, recipient hamsters were  
344 euthanized, and lung and nasal turbinate tissues collected for determination of viral load.

345

### 346 **Differential expression (DE) analysis**

347 Sequencing reads were aligned to the merged golden hamster (*Mesocricetus\_auratus*, V1.0,  
348 ENSEMBL v100) and the SARS-CoV-2 (NCBI Accession: NC\_045512.2) genomes using  
349 STAR (Dobin et al., 2013). Read counts were extracted using the "--quantMode GeneCounts"  
350 argument with STAR for each sample. Counts were used to perform differential expression  
351 (DE) with DESeq2 (Love et al., 2014). DE thresholds required genes to have log2FoldChange  
352  $\geq 1$  and a p-adjusted value  $\leq 0.05$  to be considered for downstream characterization of gene  
353 expression between conditions. Volcano plots were generated using the EnhancedVolcano R  
354 package  
355 ([www.bioconductor.org/packages/release/bioc/vignettes/EnhancedVolcano/inst/doc/Enhanced](http://www.bioconductor.org/packages/release/bioc/vignettes/EnhancedVolcano/inst/doc/EnhancedVolcano.html)  
356 [dVolcano.html](http://www.bioconductor.org/packages/release/bioc/vignettes/EnhancedVolcano/inst/doc/EnhancedVolcano.html)). Normalized viral gene counts were extracted from DESeq2 output. Boxplots  
357 were generated with ggplot2 R package (Wickham, 2016). All analysis was performed through  
358 R 4.0 with custom R script.

359

### 360 **Principal component analysis**

361 Log2FoldChange values for hamster DEGs for infections with each of the five isolates,  
362 contrasted to samples from uninfected animals, were extracted from the results of DESeq2.  
363 PCA analysis was performed on these values using the prcomp function from the stats R  
364 package. Scatterplots of PCA outputs were generated using the ggplot2 R package.

365

### 366 **Evolutionary analysis**

367 The lack of annotation regarding mechanisms underlying the regulation of many biological  
368 networks in hamsters required the determination of a well-annotated close relative from which  
369 to infer the biological roles of differentially expressed genes in a species with a better  
370 representation of the dynamics of the SARS-CoV-2 host response in humans. Evolutionary  
371 analysis was performed in accordance to the protocol set by the author (Hall, 2013), using  
372 MEGA X software. Briefly, IL6 gene sequence homologs were acquired through an extensive  
373 search of the ENSEMBL (v100) database and their identity verified through nBLAST.  
374 Sequences were aligned using MUSCLE, with positions with less than 95% coverage being  
375 excluded (Edgar, 2004). The evolutionary history of IL6 was inferred using the Maximum  
376 Likelihood method and Tamura 3-parameter model (Tamura, 1992).

377

### 378 **Gene set enrichment analysis (GSEA)**

379 Comprehensive lists of known mouse-hamster gene orthologues were compiled from the  
380 BioMart database (Smedley et al., 2015). Differentially expressed hamster genes which were  
381 identified to have a mouse orthologue form were retained from the orthologous gene list. These  
382 lists of orthologues were matched to genes categorized into Gene Ontology (GO) biological  
383 processes. The top 30 GO terms which were identified to have the most significant enrichment  
384 ( $FDR \leq 0.05$ ) across infected conditions were determined. A comparison between HK-95 and  
385 non-D614G isolates was also conducted. Heatmaps of significant GO groups were generated  
386 using the ComplexHeatmap R package (Gu et al., 2016).

387

### 388 **Whole viral genome sequencing:**

#### 389 **Reverse transcription and viral genome amplification using multiplex PCR**

390 Viral RNA extracted from cell cultures and nasal washes was treated using the TURBO DNA-  
391 free Kit (ThermoFisher Scientific) to remove residual host DNA, followed by synthesis of  
392 single-strand cDNA using SuperScript IV reverse transcriptase (Invitrogen). The viral cDNA  
393 was then enriched through multiplex tiling polymerase chain reaction (PCR), as described in  
394 the ARTIC network (<https://artic.network/ncov-2019>) (Supplementary material).

#### 395 **Nanopore sequencing of viral genome**

396 The input viral cDNA amplicons for individual samples were normalized to 5 ng, followed by  
397 end-repairing and adapter ligation according to official 1D sequencing protocols (SQK-  
398 LSK109, Oxford Nanopore). The libraries were sequenced on a Nanopore MinION device  
399 using an R9.4.1 flow cell for 48 hours. Nanopore sequencing data were analyzed using a  
400 modified Artic Network nCoV-2019 novel coronavirus bioinformatics protocol (Luo et al.,  
401 2020) (Supplementary material).

#### 402 **Illumina MiSeq sequencing of viral genome**

403 A total of 100 ng of multiplex PCR amplicons were subjected to library preparation and dual-  
404 indexing using a KAPA HyperPrep Kit and a Unique Dual-Indexed Adapter Kit (Roche  
405 Applied Science) in accordance with the manufacturer's instructions. Ligated libraries were  
406 then enriched by 6-cycle PCR amplification, followed by purification and size selection using  
407 AMPure XP beads (Beckman Coulter). The pooled libraries were sequenced using the MiSeq  
408 Reagent Kit V2 Nano on an Illumina MiSeq System. The Illumina MiSeq sequencing reads  
409 were then demultiplexed and mapped to the reference genome (accession number:

410 NC\_0.45512.2) using Samtools v1.7. Variants were called with Freebayes v1.0.0  
411 (<https://arxiv.org/abs/1207.3907>) with the haploid setting, with a minimum base quality and depth  
412 of coverage of Q30 and 50x, respectively.

### 413 **Phylogenetic analysis**

414 To determine the phylogenetic placement of our strains in the global phylogeny of SARS-CoV-  
415 2, a total of 100 SARS-CoV-2 genomes were downloaded from the GISAID severe acute  
416 respiratory syndrome coronavirus 2 data hub (Elbe and Buckland-Merrett, 2017). A  
417 phylogenetic tree was constructed with PhyML (v3.0) using the maximum likelihood algorithm.  
418 A best-fit substitution model for phylogenetic analysis was created using the Akaike  
419 information criterion, in which the general time reversible model with a fixed proportion of  
420 invariable sites (+I) was selected (Guindon et al., 2010). Bootstrap replicates were set at 1000x,  
421 and the maximum-likelihood phylogenetic tree was rooted on the earliest published genome of  
422 SARS-CoV-2 (accession no.: NC\_045512.2).

423

### 424 **References**

- 425 Andersen, K.G., Rambaut, A., Lipkin, W.I., Holmes, E.C., and Garry, R.F. (2020). The proximal origin of  
426 SARS-CoV-2. *Nat Med* 26, 450-452.
- 427 Becerra-Flores, M., and Cardozo, T. (2020). SARS-CoV-2 viral spike G614 mutation exhibits higher case  
428 fatality rate. *Int J Clin Pract*, e13525.
- 429 Blanco-Melo, D., Nilsson-Payant, B.E., Liu, W.C., Uhl, S., Hoagland, D., Moller, R., Jordan, T.X., Oishi, K.,  
430 Panis, M., Sachs, D., *et al.* (2020). Imbalanced Host Response to SARS-CoV-2 Drives Development of  
431 COVID-19. *Cell* 181, 1036-1045 e1039.
- 432 Chan, J.F., Yuan, S., Kok, K.H., To, K.K., Chu, H., Yang, J., Xing, F., Liu, J., Yip, C.C., Poon, R.W., *et al.*  
433 (2020a). A familial cluster of pneumonia associated with the 2019 novel coronavirus indicating person-  
434 to-person transmission: a study of a family cluster. *Lancet* 395, 514-523.
- 435 Chan, J.F., Zhang, A.J., Yuan, S., Poon, V.K., Chan, C.C., Lee, A.C., Chan, W.M., Fan, Z., Tsoi, H.W., Wen,  
436 L., *et al.* (2020b). Simulation of the clinical and pathological manifestations of Coronavirus Disease  
437 2019 (COVID-19) in golden Syrian hamster model: implications for disease pathogenesis and  
438 transmissibility. *Clin Infect Dis*.
- 439 Chen, J., Wang, R., Wang, M., and Wei, G.W. (2020a). Mutations Strengthened SARS-CoV-2 Infectivity.  
440 *J Mol Biol* S0022-2836, 30456-30453.
- 441 Chen, N., Zhou, M., Dong, X., Qu, J., Gong, F., Han, Y., Qiu, Y., Wang, J., Liu, Y., Wei, Y., *et al.* (2020b).  
442 Epidemiological and clinical characteristics of 99 cases of 2019 novel coronavirus pneumonia in Wuhan,  
443 China: a descriptive study. *Lancet* 395, 507-513.
- 444 Daniloski, Z., Guo, X., and Sanjana, N.E. (2020). The D614G mutation in SARS-CoV-2 Spike increases  
445 transduction of multiple human cell types. *bioRxiv*.
- 446 Deng, X., Gu, W., Federman, S., du Plessis, L., Pybus, O.G., Faria, N., Wang, C., Yu, G., Bushnell, B., Pan,  
447 C.Y., *et al.* (2020). Genomic surveillance reveals multiple introductions of SARS-CoV-2 into Northern  
448 California. *Science* 369, 582-587.
- 449 Dobin, A., Davis, C.A., Schlesinger, F., Drenkow, J., Zaleski, C., Jha, S., Batut, P., Chaisson, M., and  
450 Gingeras, T.R. (2013). STAR: ultrafast universal RNA-seq aligner. *Bioinformatics* 29, 15-21.
- 451 Dong, E., Du, H., and Gardner, L. (2020). An interactive web-based dashboard to track COVID-19 in real  
452 time. *Lancet Infect Dis* 20, 533-534.

453 Edgar, R.C. (2004). MUSCLE: a multiple sequence alignment method with reduced time and space  
454 complexity. *BMC Bioinformatics* 5, 113.

455 Elbe, S., and Buckland-Merrett, G. (2017). Data, disease and diplomacy: GISAID's innovative  
456 contribution to global health. *Glob Chall* 1, 33-46.

457 Fauver, J.R., Petrone, M.E., Hodcroft, E.B., Shioda, K., Ehrlich, H.Y., Watts, A.G., Vogels, C.B.F., Brito,  
458 A.F., Alpert, T., Muyombwe, A., *et al.* (2020). Coast-to-Coast Spread of SARS-CoV-2 during the Early  
459 Epidemic in the United States. *Cell* 181, 990-996 e995.

460 Forster, P., Forster, L., Renfrew, C., and Forster, M. (2020). Phylogenetic network analysis of SARS-  
461 CoV-2 genomes. *Proc Natl Acad Sci U S A* 117, 9241-9243.

462 Gong, Y.N., Tsao, K.C., Hsiao, M.J., Huang, C.G., Huang, P.N., Huang, P.W., Lee, K.M., Liu, Y.C., Yang,  
463 S.L., Kuo, R.L., *et al.* (2020). SARS-CoV-2 genomic surveillance in Taiwan revealed novel ORF8-deletion  
464 mutant and clade possibly associated with infections in Middle East. *Emerg Microbes Infect*, 1-37.

465 Gu, Z., Eils, R., and Schlesner, M. (2016). Complex heatmaps reveal patterns and correlations in  
466 multidimensional genomic data. *Bioinformatics* 32, 2847-2849.

467 Guindon, S., Dufayard, J.F., Lefort, V., Anisimova, M., Hordijk, W., and Gascuel, O. (2010). New  
468 algorithms and methods to estimate maximum-likelihood phylogenies: assessing the performance of  
469 PhyML 3.0. *Syst Biol* 59, 307-321.

470 Hall, B.G. (2013). Building phylogenetic trees from molecular data with MEGA. *Mol Biol Evol* 30, 1229-  
471 1235.

472 Hoffmann, M., Kleine-Weber, H., and Pohlmann, S. (2020). A Multibasic Cleavage Site in the Spike  
473 Protein of SARS-CoV-2 Is Essential for Infection of Human Lung Cells. *Mol Cell* 78, 779-784 e775.

474 Jaimes, J.A., Millet, J.K., and Whittaker, G.R. (2020). Proteolytic Cleavage of the SARS-CoV-2 Spike  
475 Protein and the Role of the Novel S1/S2 Site. *iScience* 23, 101212.

476 Ji, T., Chen, H.L., Xu, J., Wu, L.N., Li, J.J., Chen, K., and Qin, G. (2020). Lockdown contained the spread  
477 of 2019 novel coronavirus disease in Huangshi city, China: Early epidemiological findings. *Clin Infect*  
478 *Dis*.

479 Korber, B., Fischer, W.M., Gnanakaran, S., Yoon, H., Theiler, J., Abfalterer, W., Hengartner, N., Giorgi,  
480 E.E., Bhattacharya, T., Foley, B., *et al.* (2020). Tracking Changes in SARS-CoV-2 Spike: Evidence that  
481 D614G Increases Infectivity of the COVID-19 Virus. *Cell* 182, 812-827.

482 Lau, H., Khosrawipour, V., Kocbach, P., Mikolajczyk, A., Schubert, J., Bania, J., and Khosrawipour, T.  
483 (2020a). The positive impact of lockdown in Wuhan on containing the COVID-19 outbreak in China. *J*  
484 *Travel Med* 27.

485 Lau, S.Y., Wang, P., Mok, B.W., Zhang, A.J., Chu, H., Lee, A.C., Deng, S., Chen, P., Chan, K.H., Song, W.,  
486 *et al.* (2020b). Attenuated SARS-CoV-2 variants with deletions at the S1/S2 junction. *Emerg Microbes*  
487 *Infect* 9, 837-842.

488 Li, Q., Wu, J., Nie, J., Zhang, L., Hao, H., Liu, S., Zhao, C., Zhang, Q., Liu, H., Nie, L., *et al.* (2020). The  
489 Impact of Mutations in SARS-CoV-2 Spike on Viral Infectivity and Antigenicity. *Cell* 50092-8674, 30877-  
490 30871.

491 Liu, Y., Ning, Z., Chen, Y., Guo, M., Liu, Y., Gali, N.K., Sun, L., Duan, Y., Cai, J., Westerdahl, D., *et al.*  
492 (2020). Aerodynamic analysis of SARS-CoV-2 in two Wuhan hospitals. *Nature* 582, 557-560.

493 Love, M.I., Huber, W., and Anders, S. (2014). Moderated estimation of fold change and dispersion for  
494 RNA-seq data with DESeq2. *Genome Biol* 15, 550.

495 Luo, R., Wang, C.-L., Yat-Sing, W., Tang, C.-I., Liu, C.-M., Chi-Ming, L., and Lam, T.-W. (2020). Exploring  
496 the limit of using a deep neural network on pileup data for germline variant calling. *Nature* 2,  
497 pages220–227.

498 Mahase, E. (2020). Covid-19: WHO declares pandemic because of "alarming levels" of spread, severity,  
499 and inaction. *BMJ* 368, m1036.

500 Sanchez-Pacheco, S.J., Kong, S., Pulido-Santacruz, P., Murphy, R.W., and Kubatko, L. (2020). Median-  
501 joining network analysis of SARS-CoV-2 genomes is neither phylogenetic nor evolutionary. *Proc Natl*  
502 *Acad Sci U S A* 117, 12518-12519.

503 Smedley, D., Haider, S., Durinck, S., Pandini, L., Provero, P., Allen, J., Arnaiz, O., Awedh, M.H., Baldock,  
504 R., Barbiera, G., *et al.* (2015). The BioMart community portal: an innovative alternative to large,  
505 centralized data repositories. *Nucleic Acids Res* 43, W589-598.

506 Su, Y.C.F., Anderson, D.E., Young, B.E., Linster, M., Zhu, F., Jayakumar, J., Zhuang, Y., Kalimuddin, S.,  
507 Low, J.G.H., Tan, C.W., *et al.* (2020). Discovery and Genomic Characterization of a 382-Nucleotide  
508 Deletion in ORF7b and ORF8 during the Early Evolution of SARS-CoV-2. *mBio* 11.

509 Tamura, K. (1992). Estimation of the number of nucleotide substitutions when there are strong  
510 transition-transversion and G+C-content biases. *Mol Biol Evol* 9, 678-687.

511 Wickham, H. (2016). *ggplot2: Elegant Graphics for Data Analysis*. pringer-Verlag New York.

512 Wong, Y.C., Lau, S.Y., Wang To, K.K., Mok, B.W.Y., Li, X., Wang, P., Deng, S., Woo, K.F., Du, Z., Li, C., *et*  
513 *al.* (2020). Natural transmission of bat-like SARS-CoV-2PRRA variants in COVID-19 patients. *Clin Infect*  
514 *Dis*.

515 Wu, F., Zhao, S., Yu, B., Chen, Y.M., Wang, W., Song, Z.G., Hu, Y., Tao, Z.W., Tian, J.H., Pei, Y.Y., *et al.*  
516 (2020). A new coronavirus associated with human respiratory disease in China. *Nature* 579, 265-269.

517 Zhang, A.J., Lee, A.C., Chu, H., Chan, J.F., Fan, Z., Li, C., Liu, F., Chen, Y., Yuan, S., Poon, V.K., *et al.*  
518 (2020a). SARS-CoV-2 infects and damages the mature and immature olfactory sensory neurons of  
519 hamsters. *Clin Infect Dis*.

520 Zhang, L., Jackson, C.B., Mou, H., Ojha, A., Rangarajan, E.S., Izzard, T., Farzan, M., and Choe, H. (2020b).  
521 The D614G mutation in the SARS-CoV-2 spike protein reduces S1 shedding and increases infectivity.  
522 *bioRxiv*.

523 Zhang, X., Tan, Y., Ling, Y., Lu, G., Liu, F., Yi, Z., Jia, X., Wu, M., Shi, B., Xu, S., *et al.* (2020c). Viral and  
524 host factors related to the clinical outcome of COVID-19. *Nature* 583, 437-440.

525 Zhou, P., Yang, X.L., Wang, X.G., Hu, B., Zhang, L., Zhang, W., Si, H.R., Zhu, Y., Li, B., Huang, C.L., *et al.*  
526 (2020a). A pneumonia outbreak associated with a new coronavirus of probable bat origin. *Nature* 579,  
527 270-273.

528 Zhou, Z., Ren, L., Zhang, L., Zhong, J., Xiao, Y., Jia, Z., Guo, L., Yang, J., Wang, C., Jiang, S., *et al.* (2020b).  
529 Heightened Innate Immune Responses in the Respiratory Tract of COVID-19 Patients. *Cell Host*  
530 *Microbe* 27, 883-890 e882.

531

532 **Acknowledgements**

533 The authors would like to thank Dr Jane Rayner for critical reading and editing of the  
534 manuscript. This study is partly supported by the Theme-Based Research Scheme (T11/707/15)  
535 and General Research Fund (17107019) of the Research Grants Council, Hong Kong Special  
536 Administrative Region, China, and the Sanming Project of Medicine in Shenzhen, China (No.  
537 SZSM201911014).

538

539 **Author contribution**

540 B.W.M. and H.C. designed the studies; B.W.M., C.J.C., S-Y.L., S.D., P.C., A.J.Z., A.C-Y.L.,  
541 H.L., S.L., T.T-L.N., H-Y.L., E.L-K.L., K.S-S.L.,P.W. and K-H.C. performance experiments;  
542 B.W.M., C.J.C., S-Y.L., A.J.Z., K.K-W.T., J.F-W.C, K-Y.Y., G.K-H.S., and H.C. analyzed the  
543 data; B.W. M., C. J.C., G. K-H. S. and H.C. wrote the paper.

544 **Competing Interests statement**

545 The authors declare no conflict of interests.

546

547

548

549

550

551

Table 1. Sequence diversity in SARS-CoV-2 isolates

SITE	Wuhan-Hu-1	8	13	15	92	95	AA	ORF	Occurrence frequency §
241	C	-	-	-	-	T	--	UTR	>50
1515	A	-	-	-	G	-	H417R	Orf1a	17
3037	C	-	-	-	-	T	--	Orf1a	>50
4093	C	-	-	-	C/T*	-	--	Orf1a	1
4899	A	-	-	-	A/G*	-	H1545R	Orf1a	0
5310	C	C/T*	-	-	-	-	T1682I	Orf1a	12
8092	C	T	-	-	-	-	--	Orf1a	7
9223	C	-	-	-	T	-	--	Orf1a	20
10981	G	-	-	G/T‡	-	-	--	Orf1a	0
11083	G	T	-	-	T	-	L3606F	Orf1a	>50
12565	G	-	-	-	T	-	Q4100H	Orf1a	0
14408	C	-	-	-	-	T	P314L	Orf1b	>50
14805	C	-	-	-	T	-	--	Orf1b	>50
17247	T	-	-	-	C	-	--	Orf1b	>50
17423	A	-	G	G	-	-	Y1319C	Orf1b	>50
20667	A	-	G	-	-	-	--	Orf1b	1
21137	A	A/G†	-	-	-	-	K2557R	Orf1b	33
23403	A	-	-	-	-	G	D614G	S	>50
26144	G	-	-	-	T	-	G251V	Orf3a	>50
27920	C	-	C/T‡	-	-	-	--	Orf8	1
28854	C	-	T	T	-	-	S194L	N	>50

\* Reported variants with variant frequency between 10% - 30%.

† Reported variants with variant frequency 10% or below

‡ Variant frequency varies between samples derived from the same isolate

§ Data were retrieved on August 6, 2020 from GenBank

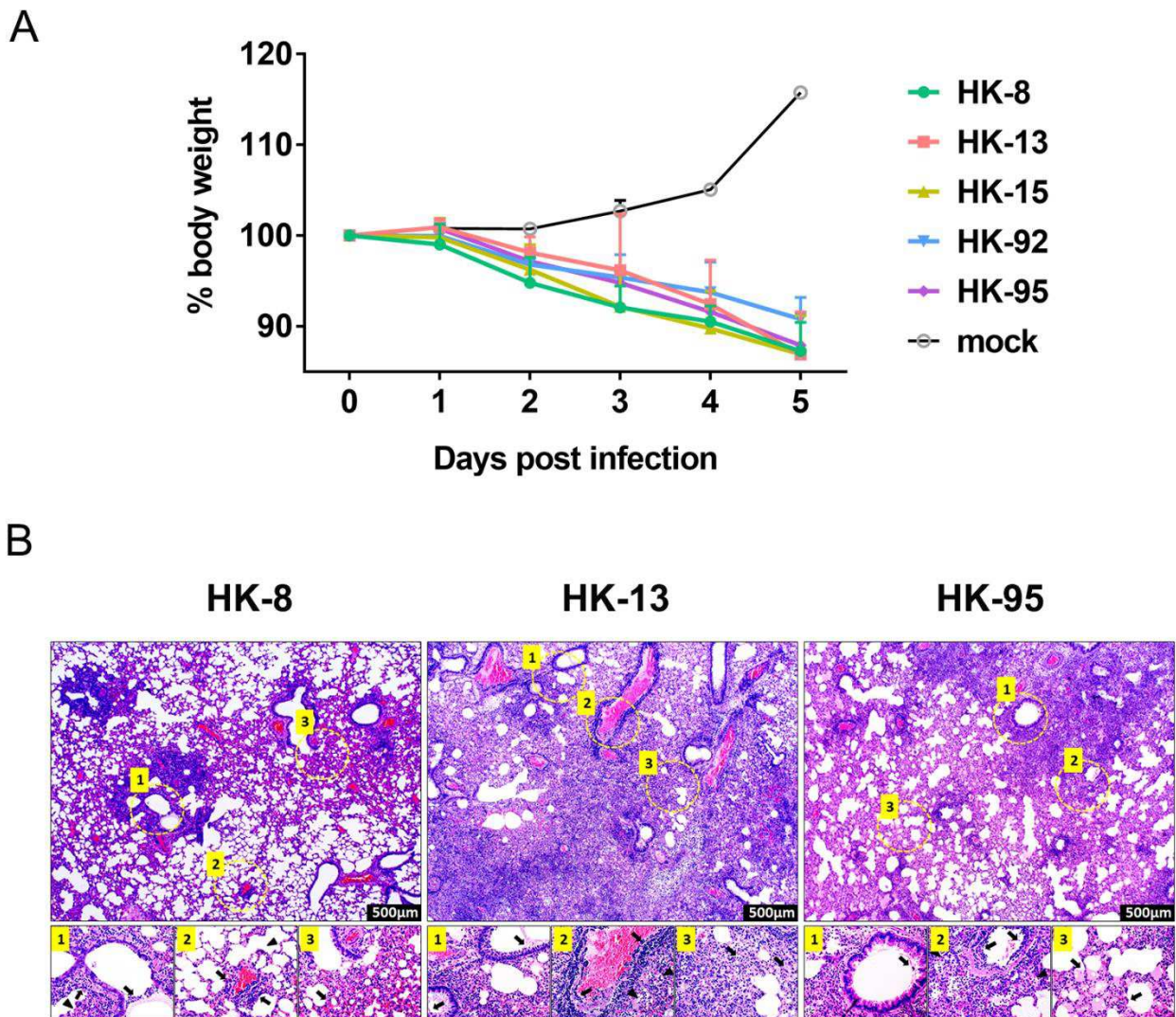
552

553

554

555 **Figure 1**

556



557

558 **Figure 1. Body weight and histopathological changes in golden Syrian hamsters**

559 **challenged with different strains of SARS-CoV-2.** (A) Body weight change in hamsters after

560 viral infection. Body weights of virus-infected and mock-infected hamsters (n=3) were

561 monitored daily for 5 days. Data are shown as the mean  $\pm$  SD percentages of the starting weight.

562 (B) Haematoxylin and eosin (H&E) staining of lung sections from SARS-CoV-2 (HK-8, HK-

563 13 and HK-95) infected hamsters, collected at 5 days post-infection (dpi). The lower

564 photographs depict higher magnification images of the regions denoted by circles in upper

565 photographs (upper photographs = 500x magnification). **HK-8:** Upper panel shows patchy

566 inflammatory damage with areas showing peribronchiolar and perivascular infiltration, blood

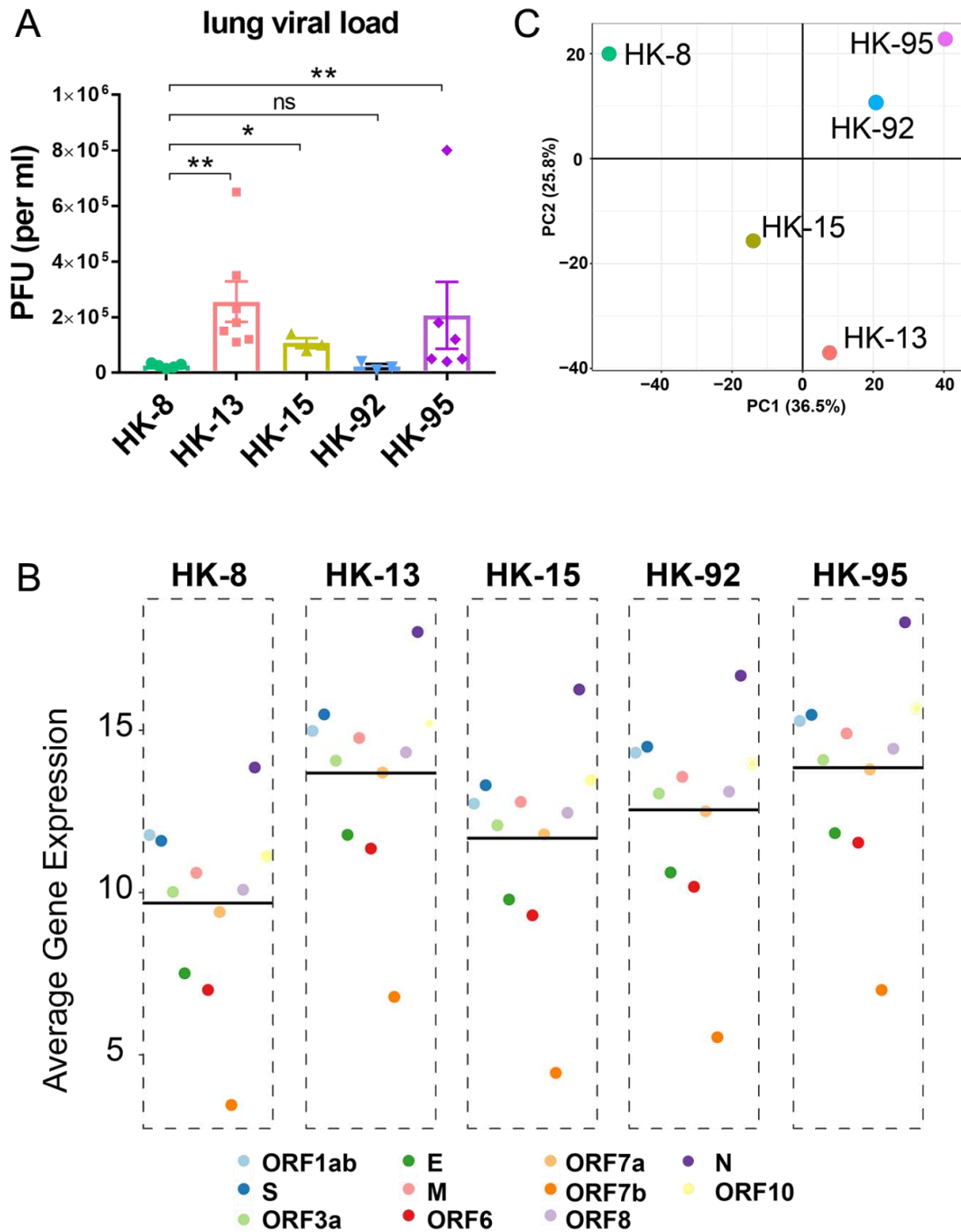
567 vessel congestion and areas of alveolar wall thickening, while alveolar exudation and  
568 infiltration were not apparent. Lower panel: (1) bronchiolar luminal exudation with cell debris  
569 (arrows), surrounding alveolar wall infiltration (arrowhead); (2) a small sized blood vessel  
570 shows perivascular and endothelial infiltration (arrows), but the surrounding alveolar space  
571 shows no infiltration or exudation (arrowhead); (3) alveolar wall capillary congestion and  
572 moderate infiltration (arrow). **HK-13:** Upper panel shows diffuse lung tissue inflammatory  
573 damage with massive alveolar space infiltration and exudation; perivascular infiltration and  
574 endothelial infiltration can be observed in all blood vessels in this lung section. Lower panel:  
575 (1) mild bronchiolar luminal exudation with cell debris (arrows); (2) a large blood vessel shows  
576 severe endothelial infiltration and vessel wall infiltration (arrows) and surrounding alveolar  
577 space infiltration and exudation (arrowheads); (3) alveolar structure destroyed by septal edema  
578 and alveolar space infiltration and fluid exudation (arrows). **HK-95:** Upper panel shows diffuse  
579 lung tissue damage with massive alveolar space exudation and infiltration; all blood vessels in  
580 the field show perivascular infiltration and endothelial infiltration. A moderate degree of  
581 bronchiolar epithelial cell death and luminal exudation is seen. Lower panel: (1) bronchiolar  
582 luminal exudation with cell debris (arrow); (2) a medium sized blood vessel shows severe  
583 endothelial infiltration and vessel wall infiltration (arrows), with alveolar space infiltration in  
584 alveoli surrounding the vessel (arrowheads); (3) alveolar structure has reduced cellularity but  
585 shows alveolar septal edema and alveolar space fluid exudation (arrows).

586

587 **Figure 2**

588

589



590

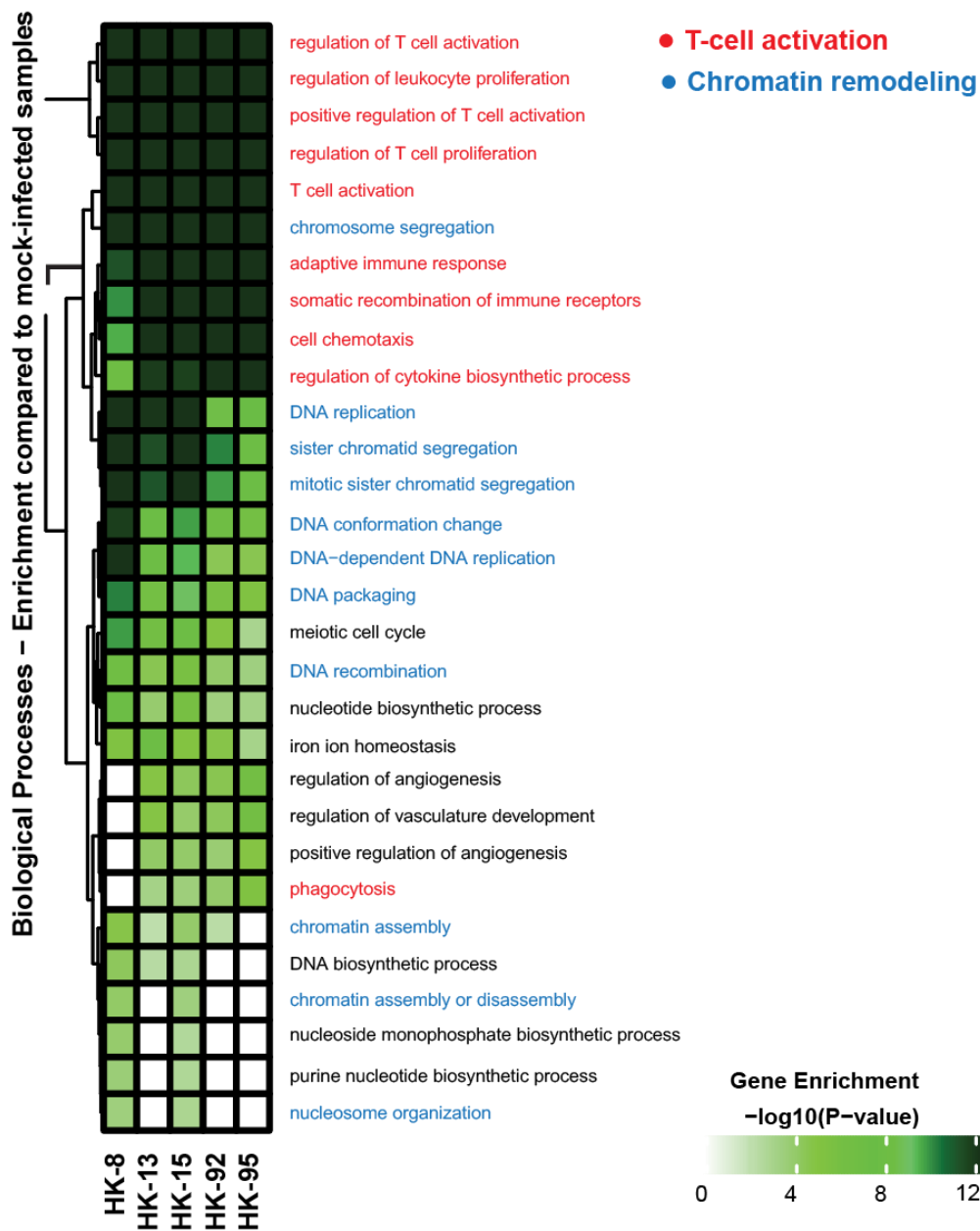
591

592 **Figure 2. Viral replication and transcriptome response to different SARS-CoV-2 isolates**  
593 **in hamster lungs.** (A) Virus replication in hamsters infected with different SARS-CoV-2

594 isolates. Three to seven hamsters per group were euthanized on day 5 post-infection for viral  
595 titration. Virus titers in lungs were determined by plaque assays (PFU/ml) and displayed as  
596 mean ( $\pm$  SEM). (B) Average viral gene expression in samples from hamsters infected with each  
597 isolate. Horizontal black lines indicate the overall mean of average expression values for viral  
598 genes per isolate. (C) Transcriptome response to different SARS-CoV-2 isolates in hamster  
599 lungs. Principal component analysis of global transcription profiles of significantly expressed  
600 host genes for infections with each isolate, compared to uninfected conditions. Individual data  
601 points and means  $\pm$  SEM are also shown. Statistical significance was calculated by Mann  
602 Whitney Wilcoxon Test; \* denotes  $p < 0.05$ , \*\* denotes  $p < 0.005$  and ns denotes *non-significant*.  
603



613 **Figure 4**

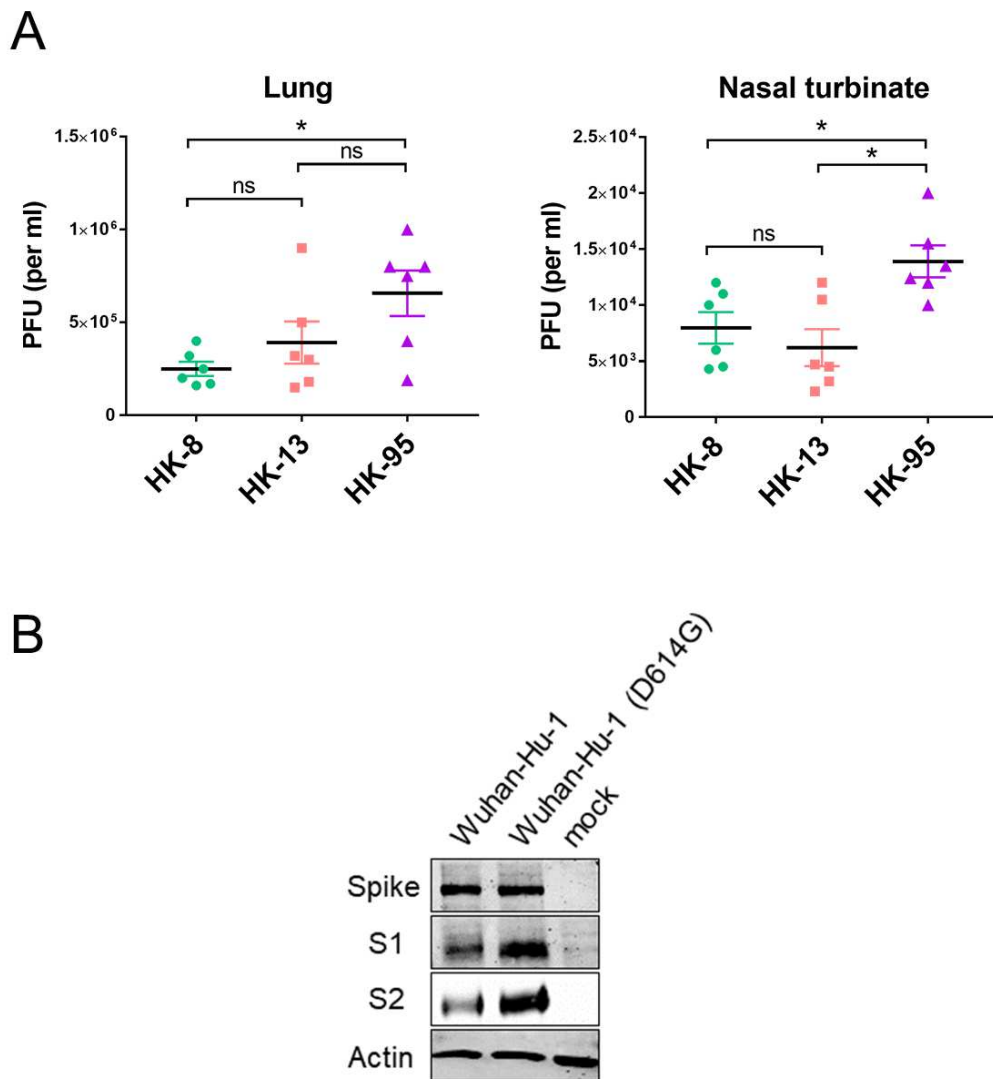


614

615

616 **Figure 4. Differential gene expression in SARS-CoV-2 infection.**

617 Heatmap depicting the expression levels of enriched gene sets in lungs collected from hamsters  
 618 infected with the indicated viruses at 5 dpi. Gene enrichment was performed on differentially  
 619 expressed genes identified in comparisons between infections with each of the 5 different  
 620 SARS-CoV-2 isolates and uninfected controls. DEGs that were identified as hamster–mouse  
 621 orthologues were extracted and matched to gene members of mouse GO biological processes.  
 622 The top 30 GO biological processes with significant enrichment ( $FDR \leq 0.05$ ) across infected  
 623 conditions are displayed.



625

626

627 **Figure 5. D614G enhances efficiency of spike protein cleavage and transmission of**  
 628 **SARS-CoV-2 isolates in hamsters.**

629 (A) Transmission of SARS-CoV-2 isolates. For each isolate, two groups of three naïve  
 630 hamsters were each co-housed with one inoculated donor on day 1 post-infection. Viral loads  
 631 (PFU/ml) in lungs and nasal turbinates of naïve contact hamsters (n=6 per isolate) at 3 days  
 632 after exposure are shown. Data are presented as individual data points and means ± SEM.  
 633 Statistical significance was calculated by Mann Whitney Wilcoxon Test; (\*) p value < 0.05, ns  
 634 – not significant. (B) The human codon-optimized spike gene of Wuhan-Hu-1 SARS-CoV-2  
 635 was cloned into the Flag-tagged-pCAGEN vector. A pCAGEN-S-D614G-Flag mutant was  
 636 constructed using a QuikChange site-directed mutagenesis kit (Agilent) according to the

637 standard protocol. Protein expression and cleavage in transfected HEK293T-ACE2 cells was  
638 demonstrated with western blotting. Rabbit anti-Spike RBD was used to detect the spike and  
639 S1 proteins, and mouse anti-Flag M2 to detect S2 protein (Supplementary materials).  
640

# Figures

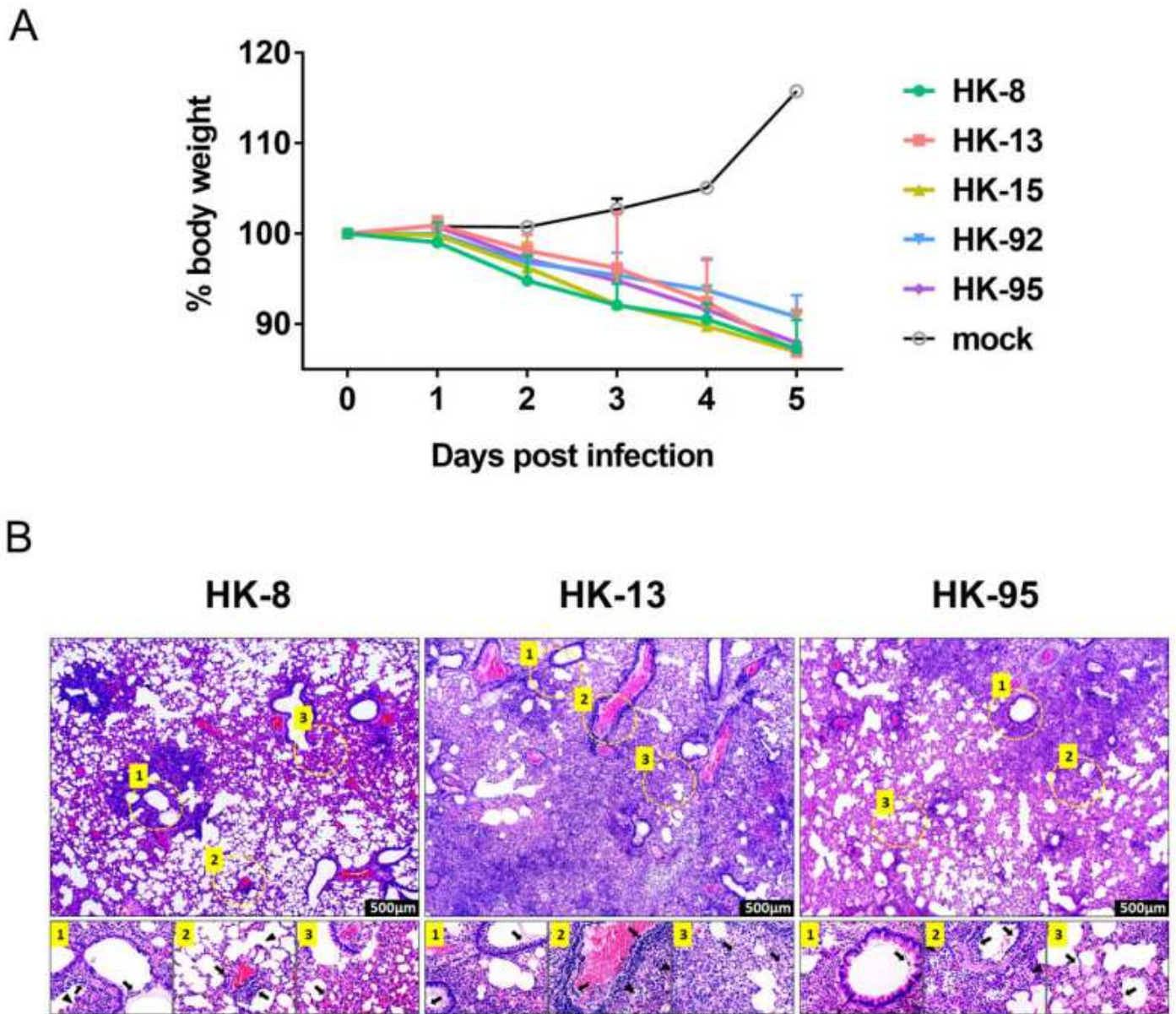


**Figure 1**

Body weight and histopathological changes in golden Syrian hamsters challenged with different strains of SARS-CoV-2. (A) Body weight change in hamsters after viral infection. Body weights of virus-infected and mock-infected hamsters (n=3) were monitored daily for 5 days. Data are shown as the mean  $\pm$  SD percentages of the starting weight. (B) Haematoxylin and eosin (H&E) staining of lung sections from SARS-CoV-2 (HK-8, HK-13 and HK-95) infected hamsters, collected at 5 days post-infection (dpi). The lower photographs depict higher magnification images of the regions denoted by circles in upper photographs (upper photographs = 500x magnification). HK-8: Upper panel shows patchy inflammatory damage with areas showing peribronchiolar and perivascular infiltration, blood vessel congestion and

areas of alveolar wall thickening, while alveolar exudation and infiltration were not apparent. Lower panel: (1) bronchiolar luminal exudation with cell debris (arrows), surrounding alveolar wall infiltration (arrowhead); (2) a small sized blood vessel shows perivascular and endothelial infiltration (arrows), but the surrounding alveolar space shows no infiltration or exudation (arrowhead); (3) alveolar wall capillary congestion and moderate infiltration (arrow). HK-13: Upper panel shows diffuse lung tissue inflammatory damage with massive alveolar space infiltration and exudation; perivascular infiltration and endothelial infiltration can be observed in all blood vessels in this lung section. Lower panel: (1) mild bronchiolar luminal exudation with cell debris (arrows); (2) a large blood vessel shows severe endothelial infiltration and vessel wall infiltration (arrows) and surrounding alveolar space infiltration and exudation (arrowheads); (3) alveolar structure destroyed by septal edema and alveolar space infiltration and fluid exudation (arrows). HK-95: Upper panel shows diffuse lung tissue damage with massive alveolar space exudation and infiltration; all blood vessels in the field show perivascular infiltration and endothelial infiltration. A moderate degree of bronchiolar epithelial cell death and luminal exudation is seen. Lower panel: (1) bronchiolar luminal exudation with cell debris (arrow); (2) a medium sized blood vessel shows severe endothelial infiltration and vessel wall infiltration (arrows), with alveolar space infiltration in alveoli surrounding the vessel (arrowheads); (3) alveolar structure has reduced cellularity but shows alveolar septal edema and alveolar space fluid exudation (arrows).

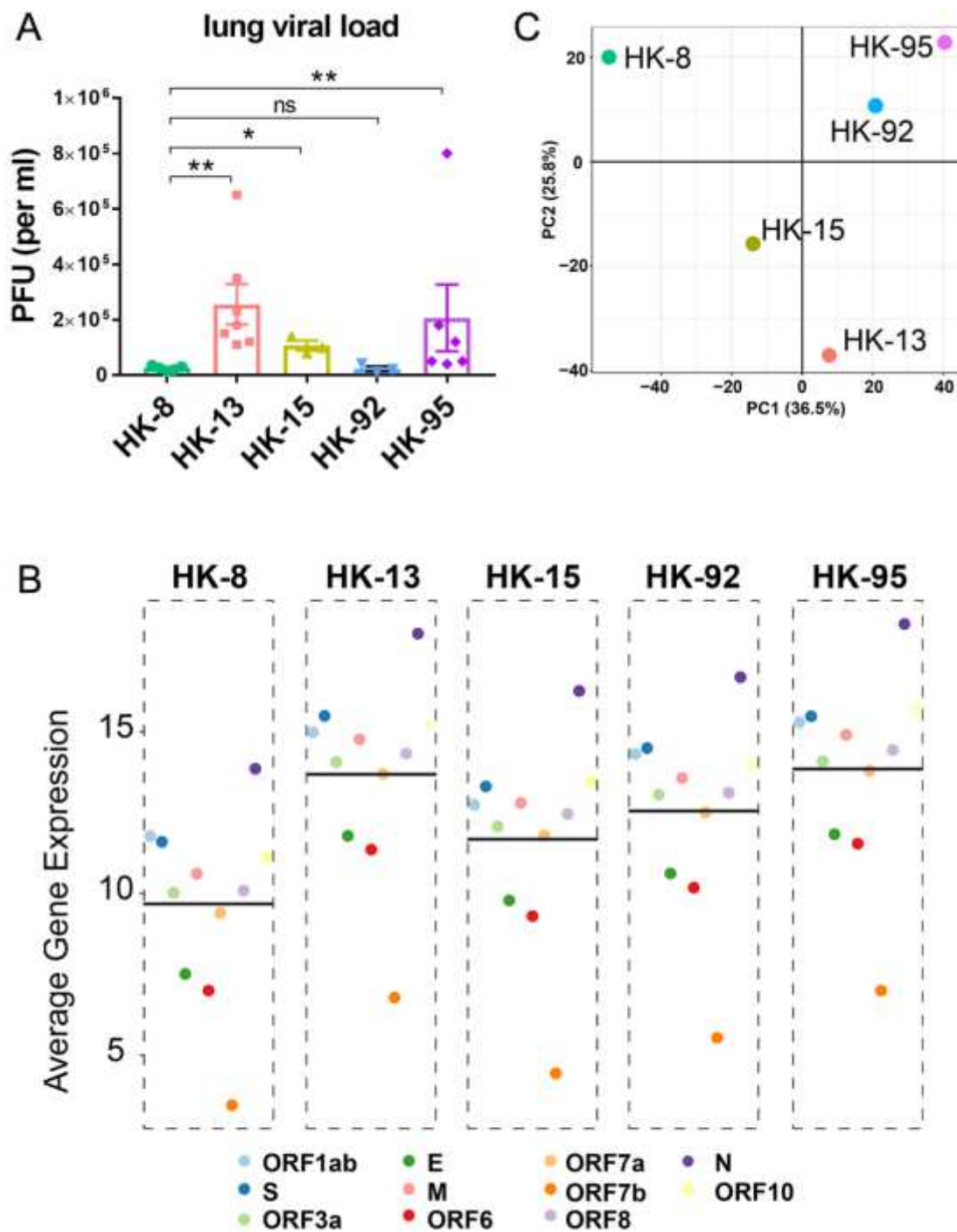


**Figure 2**

Viral replication and transcriptome response to different SARS-CoV-2 isolates in hamster lungs. (A) Virus replication in hamsters infected with different SARS-CoV-2 isolates. Three to seven hamsters per group were euthanized on day 5 post-infection for viral titration. Virus titers in lungs were determined by plaque assays (PFU/ml) and displayed as mean ( $\pm$  SEM). (B) Average viral gene expression in samples from hamsters infected with each isolate. Horizontal black lines indicate the overall mean of average expression values for viral genes per isolate. (C) Transcriptome response to different SARS-CoV-2 isolates

in hamster lungs. Principal component analysis of global transcription profiles of significantly expressed host genes for infections with each isolate, compared to uninfected conditions. Individual data points and means  $\pm$  SEM are also shown. Statistical significance was calculated by Mann Whitney Wilcoxon Test; \* denotes  $p < 0.05$ , \*\* denotes  $p < 0.005$  and ns denotes non-significant.

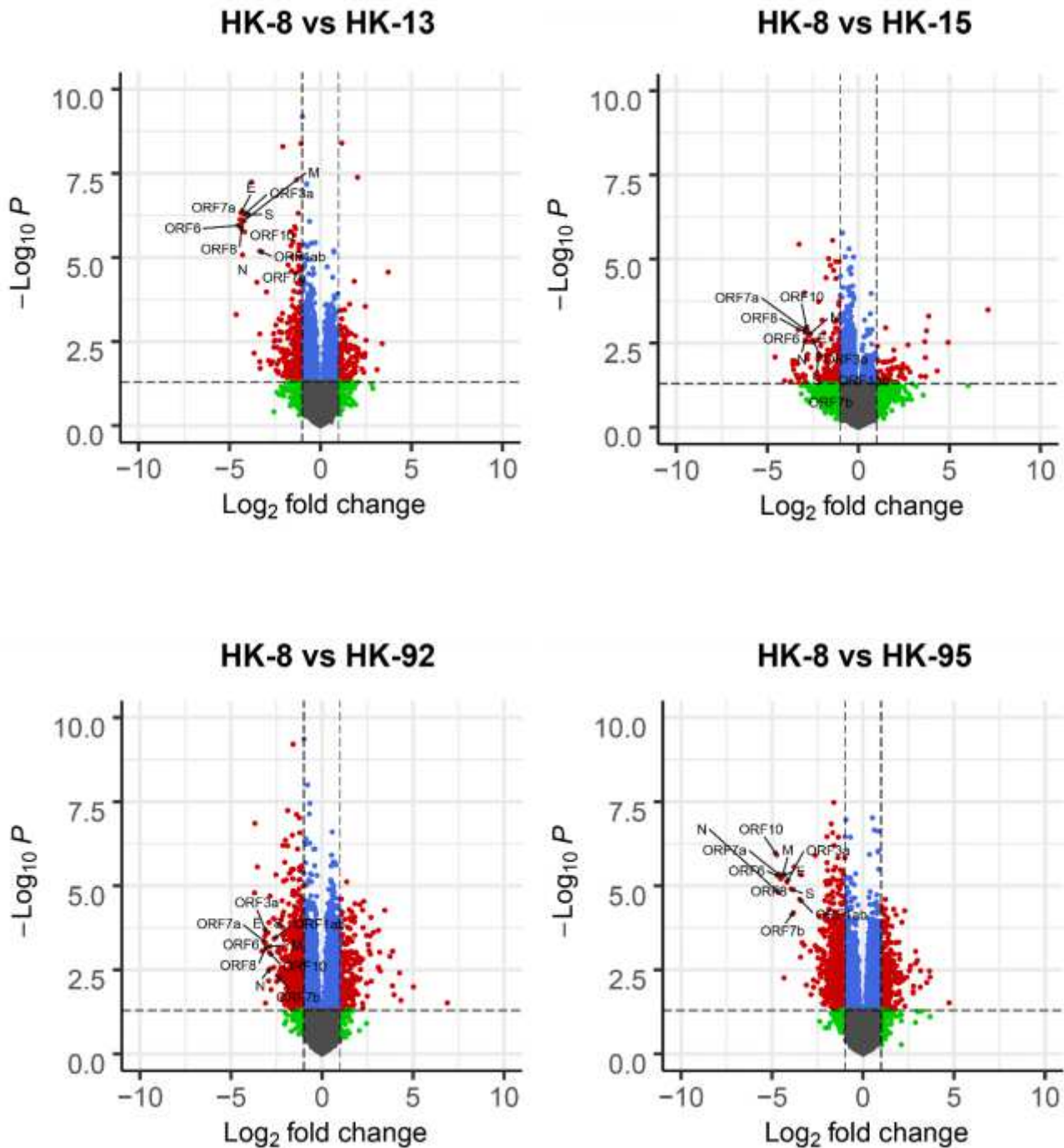


**Figure 3**

Volcano plots comparing differentially expressed genes (DEGs) in HK-8-610 infected hamster lungs to those in hamsters infected with HK-13, HK-15, HK-92 or HK-611 95. DEGs:  $\text{log}_2\text{FoldChange} \geq 1$  and  $p$ -

adjusted value  $\leq 0.05$ .

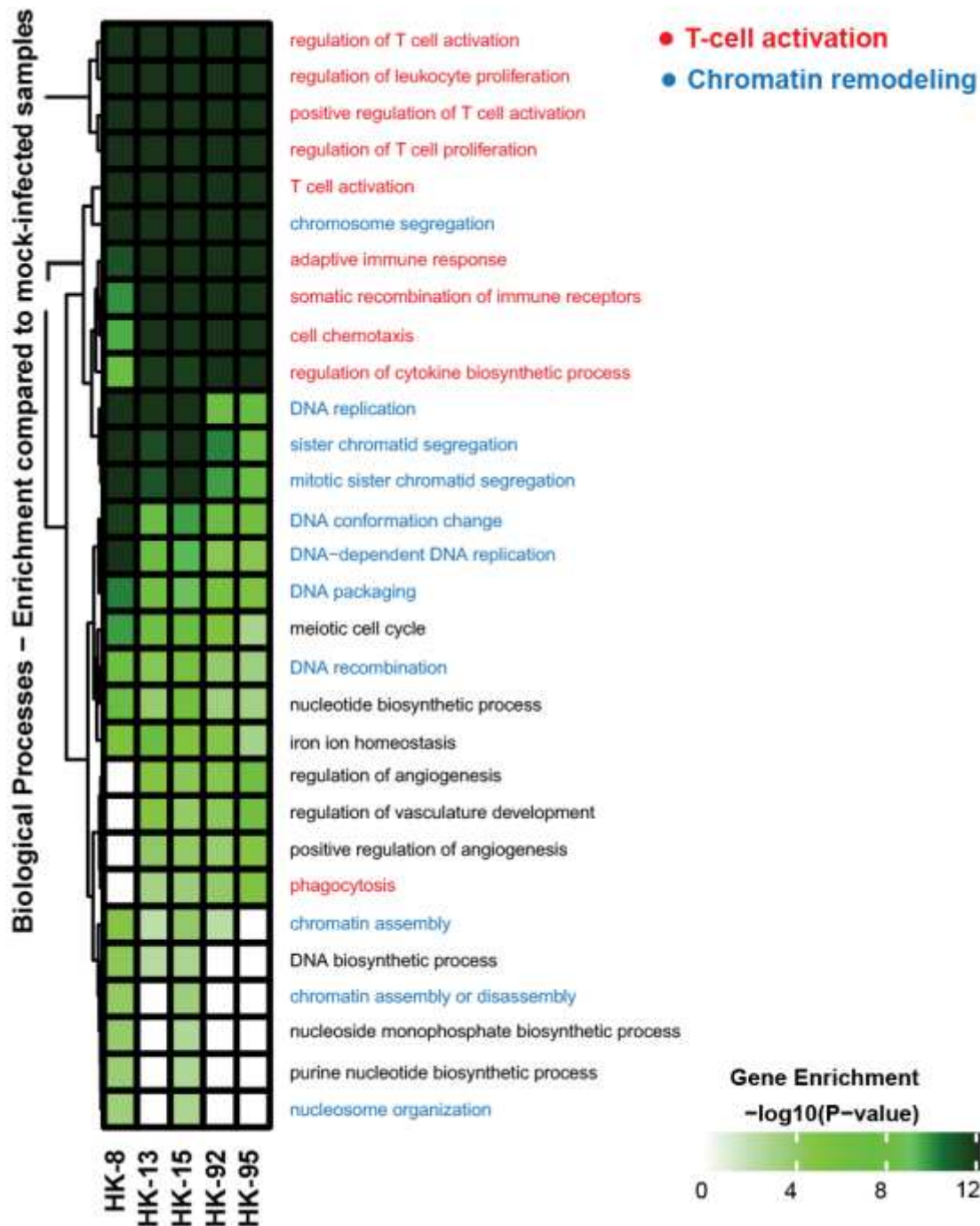
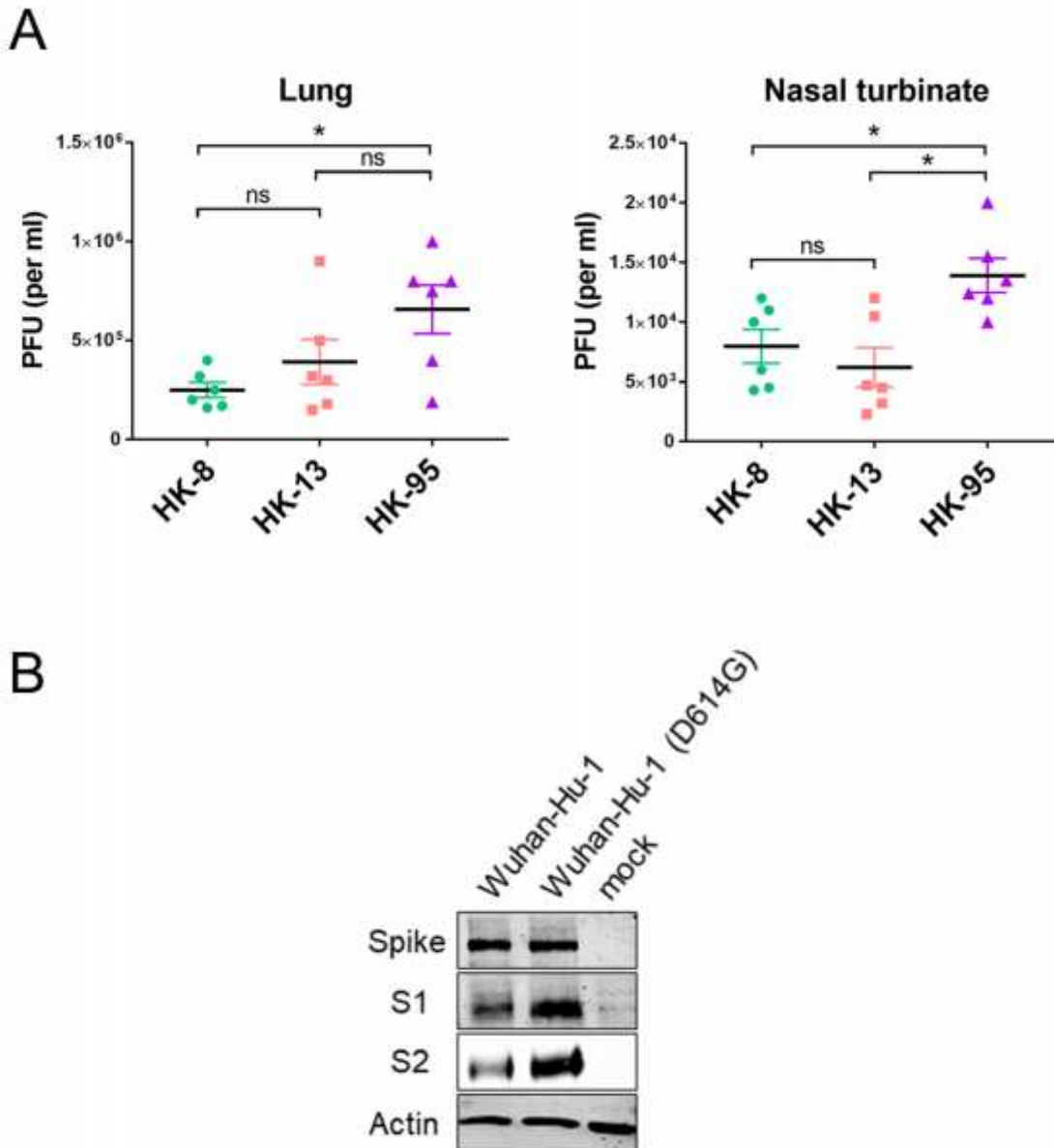


Figure 4

Differential gene expression in SARS-CoV-2 infection. Heatmap depicting the expression levels of enriched gene sets in lungs collected from hamsters 618 infected with the indicated viruses at 5 dpi. Gene enrichment was performed on differentially 619 expressed genes identified in comparisons between infections with each of the 5 different 620 SARS-CoV-2 isolates and uninfected controls. DEGs that were identified as hamster–mouse 621 orthologues were extracted and matched to gene members of mouse

GO biological processes. 622 The top 30 GO biological processes with significant enrichment ( $FDR \leq 0.05$ ) across infected 623 conditions are displayed.



**Figure 5**

Figure 5. D614G enhances efficiency of spike protein cleavage and transmission of SARS-CoV-2 isolates in hamsters. (A) Transmission of SARS-CoV-2 isolates. For each isolate, two groups of three naïve hamsters were each co-housed with one inoculated donor on day 1 post-infection. Viral loads 631 (PFU/ml) in lungs and nasal turbinates of naïve contact hamsters ( $n=6$  per isolate) at 3 days 632 after exposure are shown. Data are presented as individual data points and means  $\pm$  SEM. 633 Statistical significance was calculated by Mann Whitney Wilcoxon Test; (\*)  $p$  value  $< 0.05$ , ns 634 – not significant. (B) The human codon-optimized spike gene of Wuhan-Hu-1 SARS-CoV-2 635 was cloned into the Flag-tagged-pCAGEN vector. A pCAGEN-S-D614G-Flag mutant was 636 constructed using a QuikChange site-

directed mutagenesis kit (Agilent) according to the standard protocol. Protein expression and cleavage in transfected HEK293T-ACE2 cells was demonstrated with western blotting. Rabbit anti-Spike RBD was used to detect the spike and 639 S1 proteins, and mouse anti-Flag M2 to detect S2 protein (Supplementary materials).

## Supplementary Files

This is a list of supplementary files associated with this preprint. Click to download.

- [supplement1.pdf](#)